Visible-Light-Responsive Sillén-Structured Mixed-Cationic CdBiO₂Br Nanosheets: Layer Structure Design Promoting Charge Separation and Oxygen Activation Reactions

Hongwei Huang,[*,†,‡] Ali H. Reshak,[⊥] Sushil Auluck,[¶] Shifeng Jin,[§] Na Tian,[†] Yuxi Guo,[†] and Yihe Zhang[†]

[†]Beijing Key Laboratory of Materials Utilization of Nonmetallic Minerals and Solid Wastes, National Laboratory of Mineral Materials, School of Materials Science and Technology, China University of Geosciences, Beijing 100083, China

[‡]Department of Chemistry, The Pennsylvania State University, University Park, Pennsylvania 16802, United States

[⊥]New Technologies-Research Centre, University of West Bohemia, Univerzitni 8, 306 14 Pilsen, Czech Republic

[¶]National Physical Laboratory, Council of Scientific and Industrial Research Dr. K S Krishnan Marg, New Delhi 110012, India

[§]Beijing National Laboratory for Condensed Matter Physics, Institute of Physics, Chinese Academy of Sciences, Beijing 100190, China

S *Supporting Information*

ABSTRACT: Exploration for new layered-structured materials is of significance in multiple fields, e.g., catalysis, energy storage, and conversion, etc. In this work, we develop a visible-light-responsive Sillén-structured mixed-cationic layered catalyst CdBiO₂Br based on the typical Sillén-structured BiOBr, and first propose layer structure design as a novel tactic for promoting charge separation and oxygen activation reactions. Differing from BiOBr characterized by $[Bi_2O_2]^{2+}$ layer and interleaved Br⁻ double slabs, the crystal structure of CdBiO₂Br comprises the $[CdBiO_2]^+$ layer and interbedded single Br⁻ slice, rendering a narrowed interlayer spacing from 8.11 to 6.23 Å. The largely reduced interlayer distance drastically shortens the diffusion paths of photogenerated electrons (e⁻) and holes (h⁺) in CdBiO₂Br, allowing favorable migration of carriers from bulk to the surface of the catalysts. Profiting from this structural advantage, CdBiO₂Br presents a superior visible-light driven oxygen activation ability in evolution of superoxide radicals ($^•O_2^-$) and hydroxyl radicals ($^•OH$), with a production rate of ∼2.4 and 14.1 times that of BiOBr, respectively. DFT calculations unearth that CdBiO₂Br has smaller effective masses for both e⁻ and h⁺ than BiOBr, and meanwhile bears a significant difference in the respective mobility of e⁻ and h⁺, indicative of efficient mobility and separation of carrier charge. In particular, the h⁺ effective mass of CdBiO₂Br is merely one-third of that in BiOBr, corresponding well to the far higher $^•OH$ generation rate of CdBiO₂Br. Our work not only exposes a visible-light-active layered material for environmental chemistry/biochemistry applications but also discloses the huge potential of crystal structure manipulation in governing the charge transport behavior and photo(electro)chemical properties.
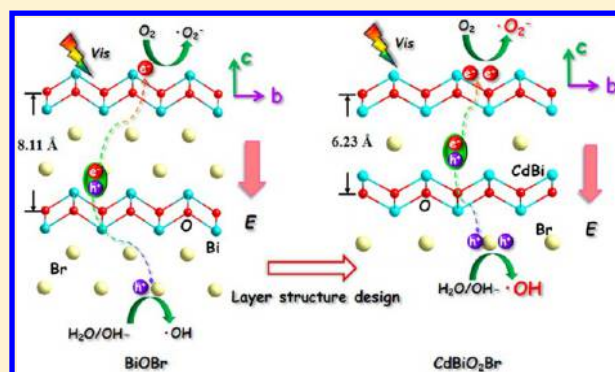
■ INTRODUCTION

Layered-structured materials exert huge potentials in diverse fields, such as catalysis, energy storage and conversion, electronics, and so on.[1−4] Layered bismuth-based (LBB) semiconductor photocatalytic materials have sparked wide-spread interests owing to their unique layered structure, strong photo-oxidative ability, and high chemical/photochemical stability.[5−9] These LBB photocatalytic materials comprise Aurivillius-structured Bi₂MO₆ (M = W, Mo, Cr),[10−12] Sillén-structured BiOX (X = Cl, Br, I),[13−15] mix-cationic Sillén-structured BiPbO₂X (X = Cl, Br),[16,17] pyrochlore-structured Bi₂MNbO₇ (M = Al, Ga, In, Fe),[18] and the newly developed Sillén-structure-related Bi₂O₂(OH)(NO₃)[19] and Bi₂O₂[BO₂(OH)].[20] Crystal structures of the LBB materials

all contain the same $[Bi_2O_2]^{2+}$ layers as the main building unit, but differ with the various interbedded ionic group or ions between $[Bi_2O_2]^{2+}$ layers. Currently, the modifications on LBB photocatalytic materials are confined to microstructure and morphology control, specific crystalline facet synthesis and hetero/homojunction construction,[21−24] and seldom efforts were made toward crystal structure design for promoting the photocatalytic performance of LBB materials. In particularly, the understanding on the relationship between crystal structure and photoreactivity is currently absent. Considering the

structural diversity, mix-cationic Sillén-structured quarternary bismuth-based materials BiMO$_2$X (M = Cd, Pb, Ca, Ba, Sr and X = Cl, Br, I), may be a good system to explore.[25,26]

It has been demonstrated that the layer structure regulation has a very large impact on the second harmonic generation (SHG) performance of layered nonlinear optical (NLO) materials.[27−29] Our group found that the cationic replacement with small atoms, like Li and Na, in layered NLO materials yields new NLO crystals Na$_2$Be$_4$B$_4$O$_{11}$ and LiNa$_5$Be$_{12}$B$_{12}$O$_{33}$ with reduced interlayer spacing, thus resulting greatly enhanced SHG intensity.[27] Besides, successes in strengthening the SHG property via layer structure design have also been achieved in other cases, such as Cs$_3$Zn$_6$B$_9$O$_{21}$[28] and Rb$_3$Al$_3$B$_3$O$_{10}$F.[29] Considering the similar layered configuration feature of LBB materials with diverse interlayer constitution, it would allow them very distinct electronic band structures, which should exert a large impact on the charge movement behavior. Therefore, exploration for new LBB photocatalytic materials for high-performance solar-energy conversion applications via layer structure design is highly fascinating and of significance.

Molecular/ionic oxygen activation for reactive oxygen species (ROS) generation are important reactions, which can produce diverse highly active and green oxidants, like superoxides ($^{\bullet}O_2^-$), singlet oxygen ($^1O_2$), hydroxyls ($^{\bullet}OH$), alkoxyl (RO−), peroxyl (RO$_2^{\bullet}$), hydrogen peroxide (H$_2$O$_2$), et.[30,31] Production of these advanced oxidants, in particular the common and efficient $^{\bullet}O_2^-$ and $^{\bullet}OH$, is the main mechanism of environmental photocatalysis and antibacterial activity. Photoinduced redox processes are thought to be the main way to ROS generation. Generally, illumination by light with photon-energy larger than band gap could induce the generation of electrons (e$^-$) in conduction band and holes (h$^+$) in valence band. Then, the e$^-$ and h$^+$ react with O$_2$/H$_2$O/ OH$^-$ to produce ROS via a series of reductive and oxidative reactions. Consequently, separation efficiency of photoinduced e$^-$ and h$^+$ is the most critical factor in ROS evolution. Lately, our group reported that macroscopic polarization enhancement in BiOIO$_3$ could largely promote the charge separation, and thus allowing strengthened oxygen activation capability for generating $^{\bullet}O_2^-$ and $^{\bullet}OH$ in abundance.[32] Thus, crystal structure engineering may be an efficient tactic for regulating the charge movement behavior and photoreactivity, and more in-depth work in this respect is anticipated.

In this work, the novel visible-light-responsive Sillén-structured CdBiO$_2$Br nanosheets with layered configuration and mixed-cations composition were developed by a soft-chemical method, and the crystal structure is determined by the powder Rietveld refinement method. Compared to BiOBr, incorporation of CdO into BiOBr results in a narrowed interlayer spacing, thus allowing CdBiO$_2$Br a much shorter diffusion path of photogenerated e$^-$ and holes h$^+$ from bulk to the surface of the catalysts. With illumination of visible light, CdBiO$_2$Br shows a more efficient performance in activating molecular/ionic oxygen for $^{\bullet}O_2^-$ and $^{\bullet}OH$ generation, in which the production rates are ~2.4 and 14.1 times that of BiOBr, respectively. DFT calculations reveal that CdBiO$_2$Br has much smaller effective masses of both e$^-$ and h$^+$ than BiOBr as well as a significant effective masse difference, indicating the e$^-$ and h$^+$ of CdBiO$_2$Br has higher mobility and separation efficiency. This work provides a promising approach to development of high-performance layered materials for solar energy conversion.

■ EXPERIMENTAL SECTION

Synthesis. The following chemicals are obtained from commercial sources and used as received: Bi(NO$_3$)$_3$·5H$_2$O (Xilong Chemical Co., Ltd.), (CH$_3$COO)$_2$Cd·2H$_2$O (Sigma-Aldrich), KBr (Beijing Chemical Co., Ltd.) and NH$_3$·H$_2$O (25%, Beijing Chemical Co., Ltd.).

CdBiO$_2$Br is synthesized by a one-pot hydrothermal process as follows: 1 mmol Bi(NO$_3$)$_3$·5H$_2$O, 1 mmol (CH$_3$COO)$_2$Cd· 2H$_2$O, and 1 mmol KBr were mixed in 30 mL of distilled water to form a homogeneous suspension under strong stirring. At the same time, the pH was controlled at 10 by drop by drop addition of NH$_3$·H$_2$O (herein, it is found that an acidic or weak alkaline synthetic environment would yield BiOBr instead of BiCdO$_2$Br, and a too high pH value of the solution will result in the presence of Bi$_2$O$_3$). After the reaction, the above mixture was transferred into a 50 mL Teflon-lined stainless autoclave, and heated at 180 °C for 12 h. The products were collected by centrifugation after cooling and washed for three times, and dried at 90 °C for 10 h.

BiOBr is also prepared by a hydrothermal route without addition of (CH$_3$COO)$_2$Cd·2H$_2$O and NH$_3$·H$_2$O. The same heating procedure was used for preparation of BiOBr.

Characterization. The X-ray diffraction (XRD) data for structural refinements were collected using a PANalytical powder X-ray diffractometer X'Pert Pro with Cu Kα radiation (40 kV, 40 mA) at ambient temperature. The data were collected over a 2θ range from 10° to 110° at intervals of 0.017° with a counting time of 1 s per step. Fast-scanning XRD data were measured on a D8 Advance X-ray diffractometer (Bruker AXS, Germany) with Cu Kα radiation (λ= 1.5418 Å). Transmission electron microscopy (TEM, JEM-2100 JEOL, Japan) and scanning electron microscopy (SEM, S-4800 Hitachi, Japan) are employed to investigate the microstructure and morphology of the products. The surface state and elemental composition were analyzed by X-ray photoelectron spectroscopy (XPS) with a VGMK II X-ray photoelectron spectrometer. Specific surface area and pore information are obtained by BET nitrogen adsorption method on a Micromeritics 3020 instrument (USA). The optical properties are investigated by UV−vis diffuse reflectance spectra (DRS) on a Varian Cary 5000 UV−vis spectrophotometer (USA).

Reactive Oxygen Species (ROS) Detection under Visible Light. The oxygen activation performance of CdBiO$_2$Br and BiOBr was determined by DMPO-assisted ESR measurement under visible light (λ > 420 nm). ESR signals of spin-trapped paramagnetic species were recorded by utilizing 5,5-dimethyl-l-pyrroline N-oxide (DMPO) as trapping agent with a Bruker A300E spectrometer. DMPO/CH$_3$OH (40 μL DMPO dissolved in 0.5 mL of CH$_3$OH) and DMPO/H$_2$O (40 μL of DMPO dissolved in 0.5 mL of deionized water) solutions were employed to inspect the superoxide radicals (DMPO−$^{\bullet}O_2^-$) and hydroxyl radicals (DMPO−$^{\bullet}OH$), respectively.[19]

Photoelectrochemical Measurements. The transient photocurrent test was conducted in a three-electrode quartz reactor with an electrochemical workstation (CHI 660E, Shanghai Chenhua). The counter electrode and the reference electrode are platinum wire and saturated calomel electrode (SCE), respectively. The CdBiO$_2$Br and BiOBr films coated on the ITO glass are employed as the working electrodes. 0.1 M Na$_2$SO$_4$ solution serves as the electrolyte. The light source is

visible light ($\lambda > 420$ nm) provided by a 300 W Xe lamp equipped with a 420 nm cutoff filter.

Theoretical Calculations. To investigate the suitability of CdBiO$_2$Br and BiOBr to be used as active photocatalysts, an *ab initio* first principle calculations are performed utilizing the full-potential method (wien2k code) within the generalized gradient approximation (PBE-GGA) to optimize the experimental lattice constant and the experimental atomic positions. The recently modified Becke-Johnson potential (mBJ) is used to calculate the ground state properties.[33,34]

The parameters that used in the *ab initio* calculations are the basis functions in the interstitial region (IR) expanded up to $R_{MT} \times K_{max} = 7.0$ and inside the atomic spheres for the wave function. $l_{max} = 10$. and the charge density is Fourier expanded up to $G_{max} = 12$ au^{-1}. Self-consistency is obtained using 4000 $\vec{k}$ points in the irreducible Brillouin zone (IBZ). The self-consistent calculations are converged since the total energy of the system is stable within 0.00001 Ry. The electronic properties are calculated using 50000 $\vec{k}$ points in the IBZ. The input required for calculating the total and partial density of states (DOS) are the energy eigenvalues and eigenfunctions which are the natural outputs a band structure calculation. Therefore, from the band structure calculation the DOS are calculated by means of the modified tetrahedron method.[35]

■ RESULTS AND DISCUSSION

Crystal Structure, Microstructure, and Elemental Composition. CdBiO$_2$Br was first reported by Sillén in 1939 and the crystal structure was determined.[36] Then, the ABiO2X (A = Cd, Ca, Sr, Ba, Pb; X = halogen) Sillen X1 Series were reported by Mentré et al. and the photoluminescence properties was investigated.[37] Here, the crystal structure of CdBiO$_2$Br is refined by powder Rietveld refinement method using the computer software General Structure Analysis System (GSAS). Figure 1 shows the Rietveld analysis patterns for X-ray
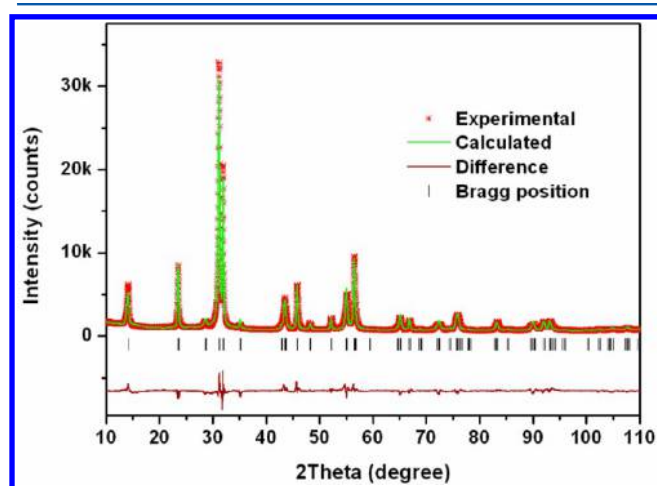

Figure 1. Rietveld refinement XRD pattern of CdBiO$_2$Br.

powder diffraction data of CdBiO$_2$Br. It crystallizes in a tetragonal $I4/mmm$ space group, and the Cd^{2+} and Bi^{3+} ions with ratio of 0.5/0.5 co-occupy in the same site (0.00000, 0.00000, 0.16148). Table 1 shows the corresponding crystallographic data and refinement parameters of CdBiO$_2$Br. The lattice parameters are refined to $a = b = 3.95668(9)$ Å, and $c = 12.4497(3)$ Å. The reliability parameters of refinement are $R_{wp} = 8.92\%$, $R_p = 6.45\%$, and $\chi^2 = 10.50$, which can confirm the

Table 1. Crystallographic Data and Refinement Parameters of CdBiO$_2$Br

| compound	CdBiO$_2$Br
space group	tetragonal-$I4/mmm$
a, Å	3.95668(9)
b, Å	3.95668(9)
c, Å	12.4497(3)
α, deg	90
V, Å^3	194.904(8)
Z	4
R_{wp}, %	8.92
R_p, %	6.45
χ^2	10.50

phase purity of the as-prepared CdBiO$_2$Br powder. The fast XRD scanning pattern (Figure S1) also accords with that of powder Rietveld refinement. The Fractional atomic coordinates, occupancies and isotropic thermal parameters are summarized in Table S1.

Because of the similarity in constitution and structure of CdBiO$_2$Br and BiOBr, their crystal structures are carefully compared. As displayed in Figure 2, the crystal structure of CdBiO$_2$Br is constructed by [CdBiO$_2$]$^+$ layers and alternatively arranged Br$^-$ ions, which is analogous to that of BiOBr consisting of [Bi$_2$O$_2$]$^{2+}$ layers and interleaved Br$^-$ slices. However, it is important to note that there is only one Br$^-$ ions slice between the two adjacent [CdBiO$_2$]$^+$ layers in CdBiO$_2$Br along the c axis, while two Br$^-$ ions slices reside in the space between two neighboring [Bi$_2$O$_2$]$^{2+}$ layers in BiOBr along the same direction (Figure 2a and b). It thus gives rise to a shorter [CdBiO$_2$]$^+$ interlayer spacing of 6.23 Å in CdBiO$_2$Br, comparing to the obviously larger one of 8.11 Å in BiOBr. The shorter interlayer spacing may favor the fast migration and diffusion of charge carriers among layers. Figure 2c and d show the [CdBiO$_2$]$^+$ and [Bi$_2$O$_2$]$^{2+}$ layers along different plane or direction, respectively. With regard to the [CdBiO$_2$]$^+$ layer, the introduction of Cd^{2+} into [Bi$_2$O$_2$]$^{2+}$ layers results in a decreased Cd/Bi–O bond length of 2.265 Å in comparison with that of Bi–O (2.320 Å). Nevertheless, the Bi–O–Bi angle is 121.76° in [CdBiO$_2$]$^+$ layer, which is larger than that in [Bi$_2$O$_2$]$^{2+}$ layer (115.32°), which leads to an expanded unit parameter along a and b axes in CdBiO$_2$Br (3.96 Å) compared to that of BiOBr (3.92 Å).

X-ray photoelectron spectroscopy (XPS) was performed to study the elemental composition and surface state of CdBiO$_2$Br. Figure 3a displays all the constituent elements Cd, Bi, O, and Br. The two peaks with binding energies of 163.93 and 158.73 eV are assigned to the Bi 4f$_{5/2}$ and Bi 4f$_{7/2}$ peaks, respectively (Figure 3b).[38] The Cd 3d$_{3/2}$ and Cd 3d$_{5/2}$ are detected at the binding energies of 411.29 and 404.55 eV, respectively (Figure 3c).[39] Figure 3d shows the Br 3d peak, which can be split into two peaks at 69.21 and 68.15 eV, corresponding to Br 3d$_{3/2}$ and Br 3d$_{5/2}$, respectively.[39] For the O 1s spectra, as shown in Figure 3e, it could be deconvoluted into two bands at 529.4 and 530.7 eV. The two peaks are attributed to the lattice oxygen and hydroxyl groups adsorbed on the surface of CdBiO$_2$Br, respectively. The XPS result confirms the presence of Cd^{2+}, Bi^{3+}, O^{2-}, and Br$^-$ in CdBiO$_2$Br.

The morphology and microstructure of CdBiO$_2$Br are studied via scanning electron microscopy (SEM) and transmission electron microscopy (TEM). CdBiO$_2$Br products are composed of numerous nanosheets with size of several
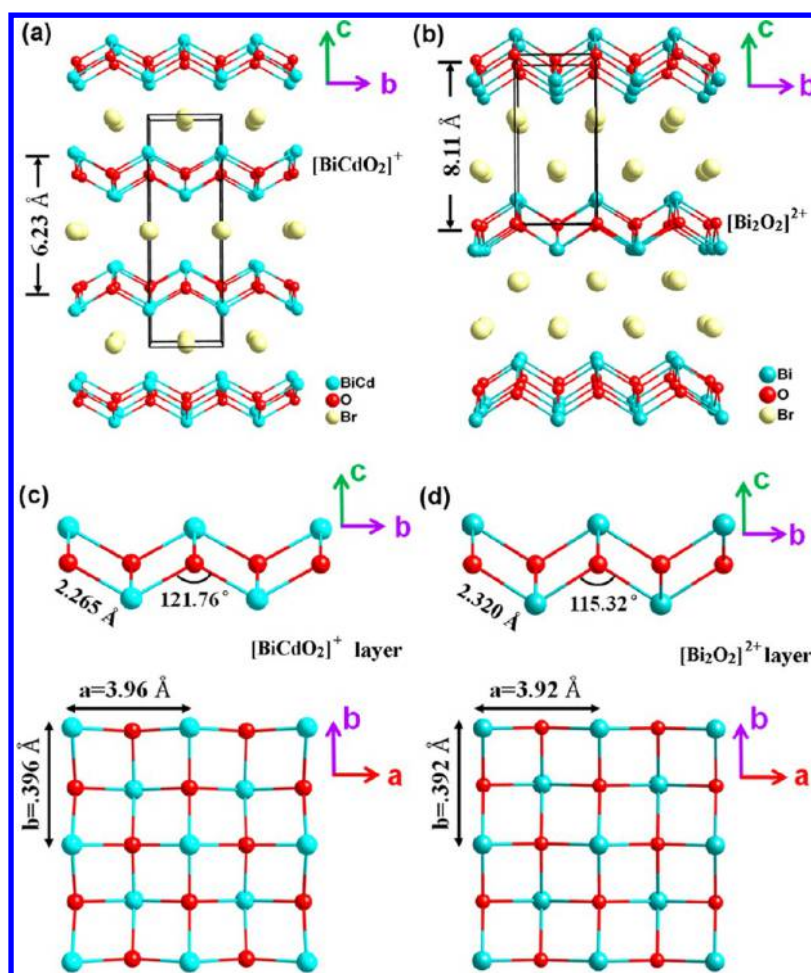
Figure 2. Crystal structures of (a) CdBiO$_2$Br and (b) BiOBr along the $b-c$ plane. (c) [CdBiO$_2$]$^+$ layer of CdBiO$_2$Br and (d) [Bi$_2$O$_2$]$^{2+}$ layer of BiOBr in different views.

hundreds of nanometers (Figure S2). TEM image confirms the square nanosheet structure of CdBiO$_2$Br with size of ~300 nm (Figure 4a). The high-resolution TEM (HRTEM) image reveals two sets of lattice fringes with an interplanar spacing of 0.280 nm (Figure 4c), which can be assigned to the {110} facets of CdBiO$_2$Br. It demonstrates that the exposing facet of CdBiO$_2$Br nanosheets is {001} facet. The corresponding selected-area electron diffraction (SAED) pattern was shown in the inset of Figure 4c, in which the angle indicated is 45°, in agreement with the theoretical angle between the {110} and {200} facets. The SAED pattern also reflects the [001] zone-axis diffraction spots of tetragonal CdBiO$_2$Br. For comparison, the TEM images of BiOBr are also provided as shown in Figure 4b and d. BiOBr also shows nanosheet morphology with similar size with CdBiO$_2$Br. The perpendicularly aligned lattice fringes with a spacing of 0.277 nm and the corresponding SAED pattern indicate that the exposed facet of BiOBr is also {001} facet. The similar crystalline size and exposing facet of CdBiO$_2$Br and BiOBr imply that these factors may not contribute to their photocatalytic activity difference.

The BET nitrogen adsorption−desorption isotherms and pore size distribution curves of CdBiO$_2$Br and BiOBr are shown in Figure 5. The both compounds have the same isotherms type, which can be assigned to type IV based on the BDDT classification. It indicates the existence of mesopores, which corresponds to the pore size distribution curves that center on 30 nm (inset of Figure 5), and the mesopores should

be due to the aggregation of the nanosheets. The BET specific surface area of CdBiO$_2$Br and BiOBr is determined to be 14.3 and 15.7 m^2/g, respectively. Thus, CdBiO$_2$Br and BiOBr have very similar specific surface area, which will also not influence their photocatalytic performance.

Electronic Band Structure, Optical Absorption, and Band Gap. Since the photocatalytic activities are directly related to the electronic structure of materials, the electronic band structure along the high symmetry directions of the first BZ and the total density of states of CdBiO$_2$Br and BiOBr are calculated to explore the bands dispersion and the nature of the fundamental energy band gap. We set the zero-point of energy (Fermi level, E$_F$) at the valence band maximum (VBM). As shown in Figure 6a, the valence band (VB) top and conduction band (CB) bottom of CdBiO$_2$Br are located at the points of M and Γ, respectively. It indicates that CdBiO$_2$Br has an indirect-transition band gap, which is calculated to be 2.77 eV. Therefore, the photogenerated electrons (e$^-$) would not recombine directly with holes (h$^+$), and it needs the assistance of phonons in order to keep momentum conservation.[40] This implies that the investigated compound may have a long lifetime of photoexcited e$^-$ and h$^+$, which can increase the probabilities for photogenerated e$^-$ and h$^+$ to participate in photocatalytic reactions. This theoretical band gap of CdBiO$_2$Br is very close to the calculated one of BiOBr (2.76 eV), as seen in Figure 6b. Besides, the electronic band structures reveal that the CB and VB of CdBiO$_2$Br and BiOBr
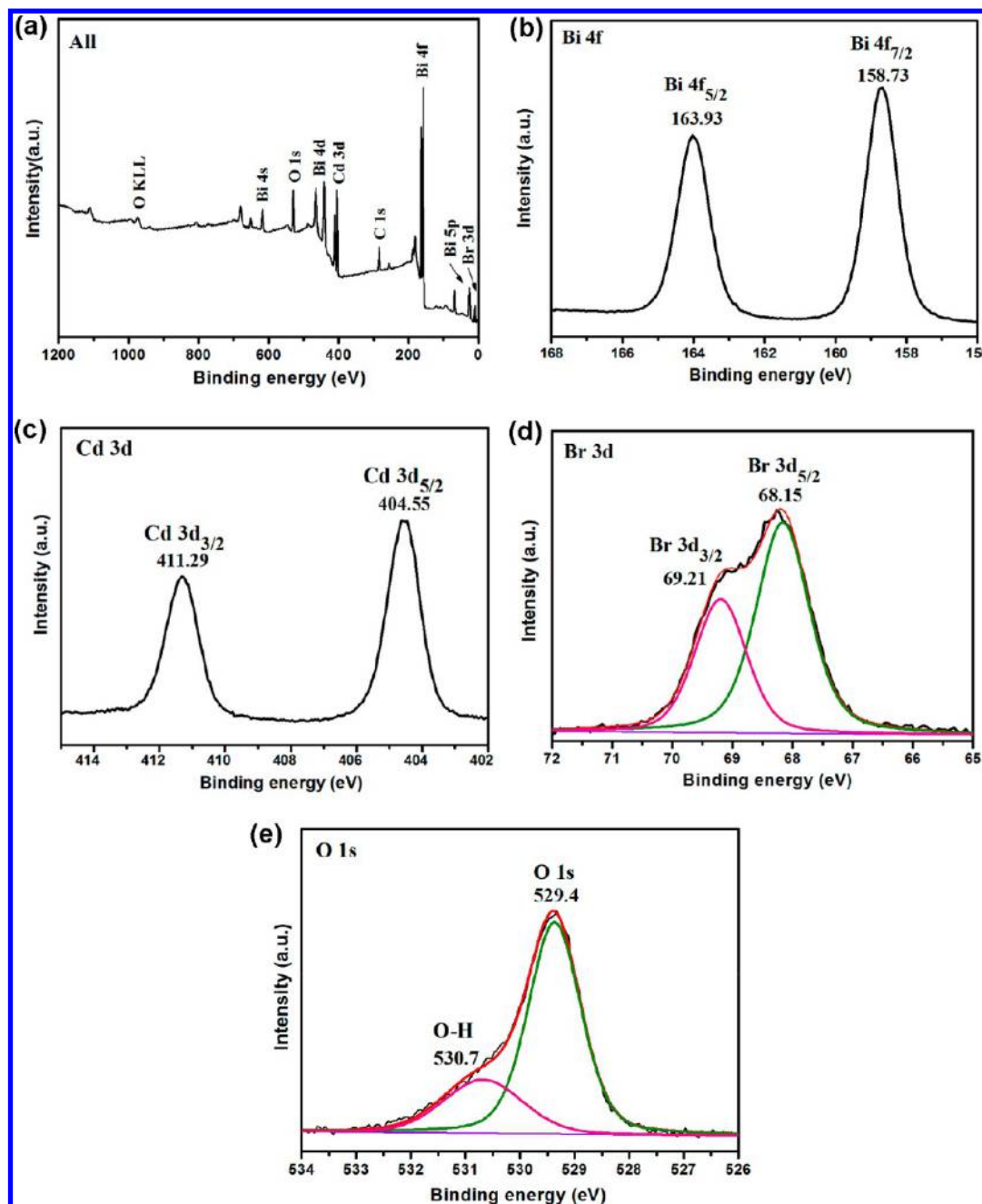
Figure 3. (a) XPS survey spectra and high-resolution (b) Bi 4f, (c) Cd 3d, (d) Br 3d, and (e) O 1s XPS spectra of CdBiO$_2$Br.

are almost situated at the same positions, suggesting that they may hold comparable photoinduced reduction and oxidation driving force.

The optical absorption and experimental band gap of CdBiO$_2$Br are determined by UV−vis diffuse reflectance spectra (DRS). As depicted in Figure 6c, CdBiO$_2$Br has an absorption edge of approximately 440 nm, which is almost same with that of BiOBr. Correspondingly, the indirect experimental band gaps of CdBiO$_2$Br and BiOBr are determined from the Kubelka−Munk and Tauc plot to be 2.76 eV (Figure 6d). This value is in very good accordance with their calculated band gap. The above theoretical and experimental results demonstrated that CdBiO$_2$Br can respond to visible light, and its photoabsorption as well as the

photoinduced reduction and oxidation ability is also comparable to those of BiOBr.

Visible-Light-Driven Molecular Oxygen Activation Performance. The visible-light responsive molecular/ionic oxygen activation properties of CdBiO$_2$Br and BiOBr are investigated by ESR, which is always employed to detect the spin-trapped paramagnetic molecular oxygen species.[8] Herein, 5,5-dimethyl-l-pyrroline N-oxide (DMPO) serves as the trapping agent, and the superoxide radicals (•O$_2^-$) and hydroxyl radicals (•OH) are inspected, respectively, in methanol and water. As seen from Figure 7a, both CdBiO$_2$Br and BiOBr show a set of four identical peaks with illumination of visible light ($\lambda > 420$ nm), demonstrating the appearance of superoxide radicals adduct DMPO−•O$_2^-$ which is attributed to the reduction of O$_2$ molecule by photogenerated electrons.[41]
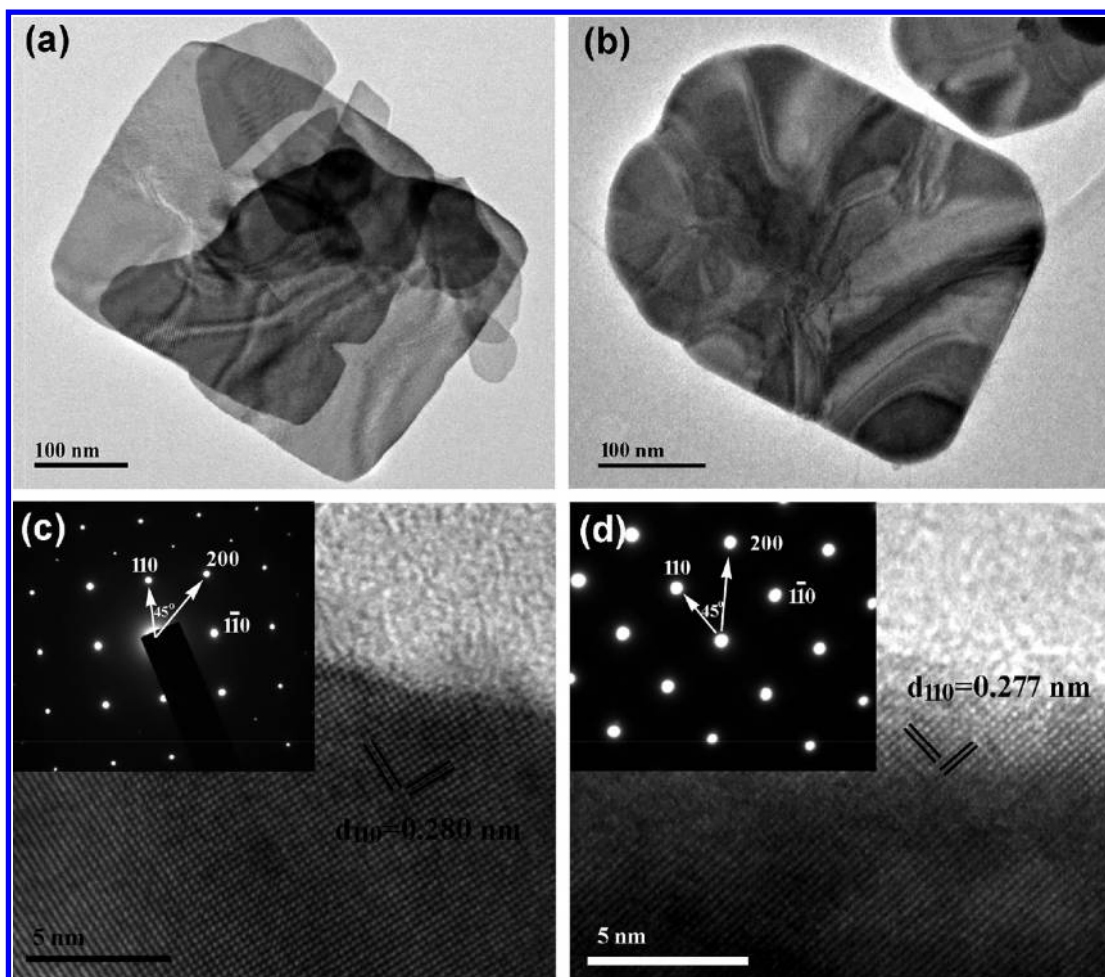
Figure 4. TEM images of (a) CdBiO$_2$Br and (b) BiOBr. HRTEM images of (c) CdBiO$_2$Br (inset is the SAED pattern) and (d) BiOBr (inset is the SAED pattern).
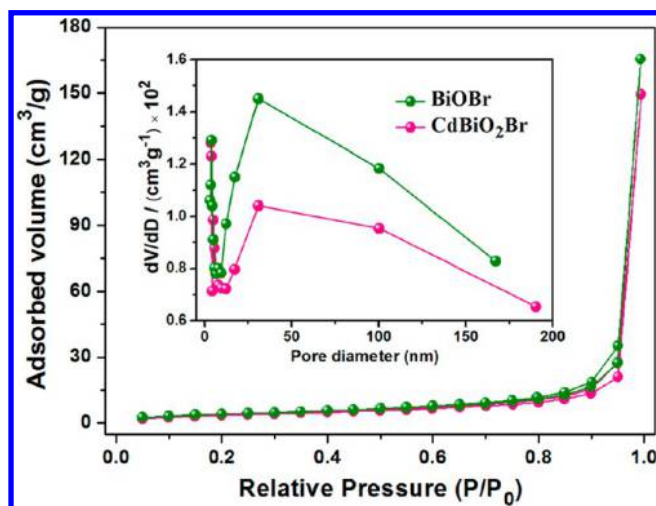

Figure 5. Nitrogen adsorption−desorption isotherms and pore-size distribution curves (inset) of CdBiO$_2$Br and BiOBr.

Remarkably, the peak intensity of CdBiO$_2$Br is obviously higher than that of BiOBr, revealing that CdBiO$_2$Br can produce more $^{\bullet}$O$_2^{-}$ than BiOBr. Figure 7b shows the signal pattern for detection of $^{\bullet}$OH produced from CdBiO$_2$Br and BiOBr. A four-peaks spectrum with peak intensities of 1:2:2:1 that is assigned to the DMPO−$^{\bullet}$OH appear for both materials under visible

light, which reveals that both CdBiO$_2$Br and BiOBr can convert H$_2$O/OH$^-$ into $^{\bullet}$OH through oxidation reaction of photo-induced holes. Similarly, the DMPO−$^{\bullet}$OH signal produced by CdBiO$_2$Br is also much stronger than that of BiOBr, indicating the stronger ability of CdBiO$_2$Br in $^{\bullet}$OH evolution. For further confirmation, the quantitative comparison on radical amount is conducted. According to the quantitative relation that the radical amount is in proportion to the square of signal intensity,[32,42] the production amounts of $^{\bullet}$O$_2^{-}$ and $^{\bullet}$OH over CdBiO$_2$Br are ~2.4 and 14.1 times that of BiOBr, respectively. These results illustrate that CdBiO$_2$Br has a far superior ability in molecular/ionic oxygen activation for producing highly oxidative $^{\bullet}$O$_2^{-}$ and $^{\bullet}$OH.

Investigation on Charge Separation, Movement Behavior, and Effective Mass of Carriers. To explore the origin for superior visible-light active ROS evolution performance of CdBiO$_2$Br, the factors that are closely related to photocatalytic activity are considered. As the specific surface area, optical absorption and band edge level of CdBiO$_2$Br and BiOBr show no big difference, charge separation efficiency should be the dominant factor for their distinct molecular oxygen activity difference.

Transient photocurrent response under visible light (λ > 420 nm) was utilized to monitor the charge separation efficiency of CdBiO$_2$Br and BiOBr.[32] As shown in Figure 8, reproducible photocurrent swiftly generates and disappears with light on and
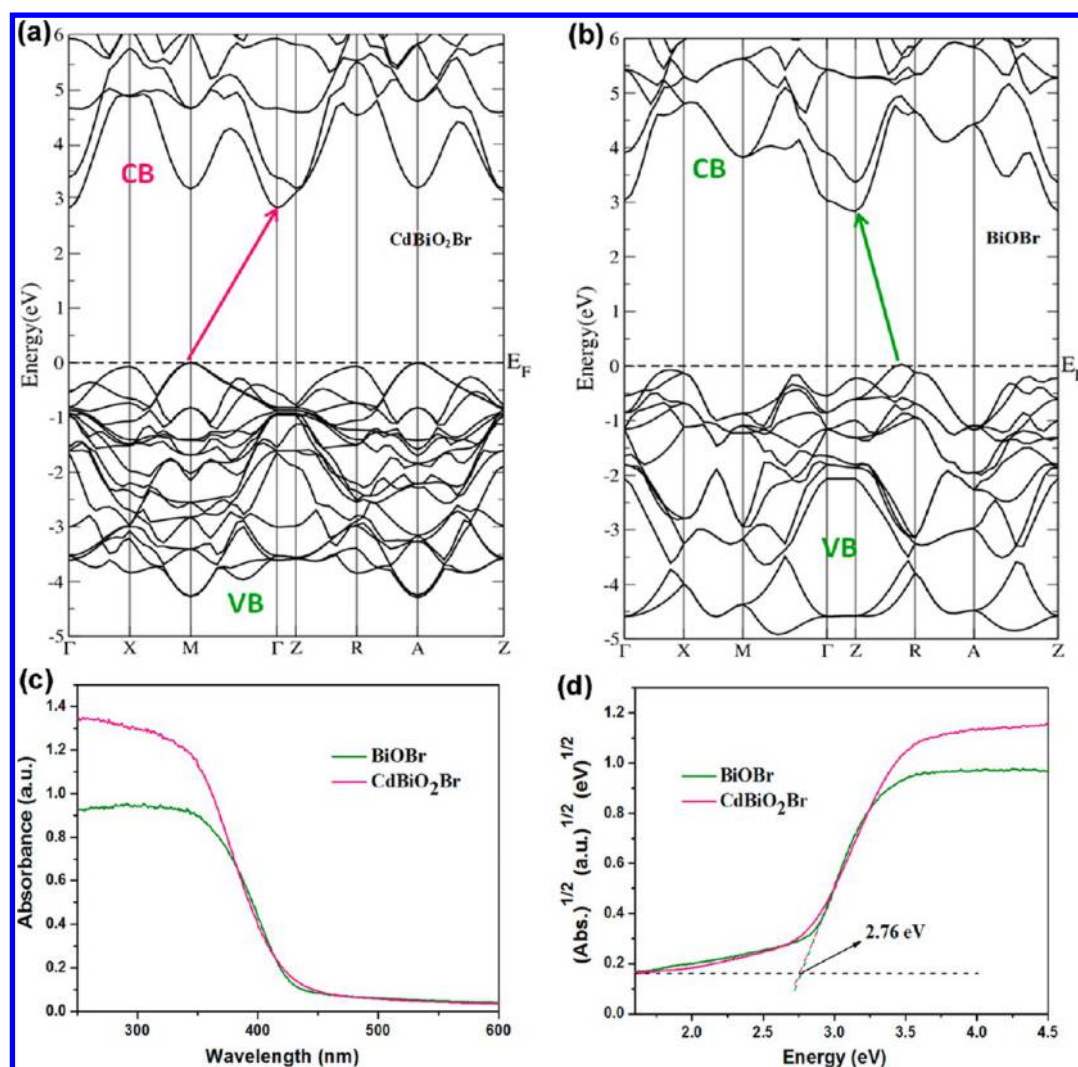
Figure 6. Electronic band structures of (a) CdBiO$_2$Br and (b) BiOBr. UV−vis diffuse reflectance spectra (DRS) (c) and the Kubelka−Munk and Tauc plot (d) of CdBiO$_2$Br and BiOBr.
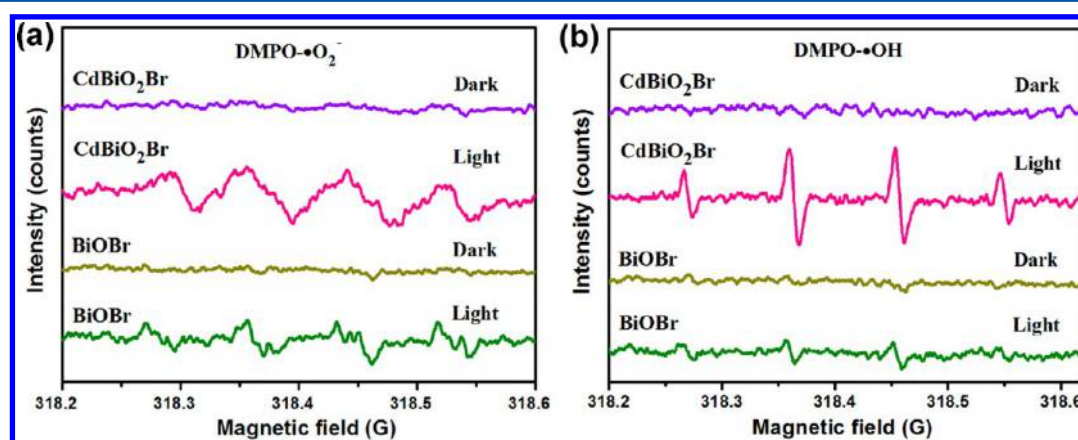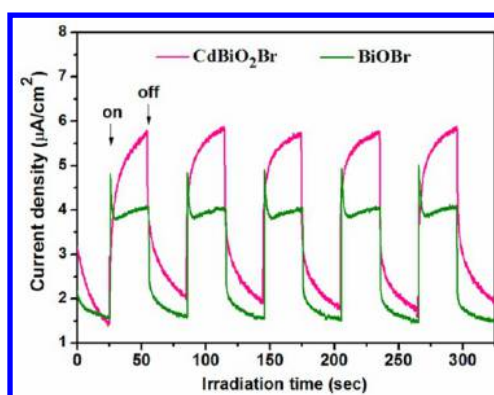

Figure 7. ESR signals for (a) DMPO−•O$_2$$^-$ and (b) DMPO−•OH over CdBiO$_2$Br and BiOBr under visible light irradiation (λ > 420 nm).

off for both electrodes, demonstrating they are visible light activated and photochemically stable. It is obvious to notice that CdBiO$_2$Br displays steady photocurrent production, whereas photocurrent decay was observed for BiOBr which should be attributed to the recombination of photogenerated e$^-$ and h$^+$, and the current density of CdBiO$_2$Br is ∼1.5 times that

of BiOBr. It uncovers the fact that more efficient charge separation occurs in CdBiO$_2$Br than in BiOBr.
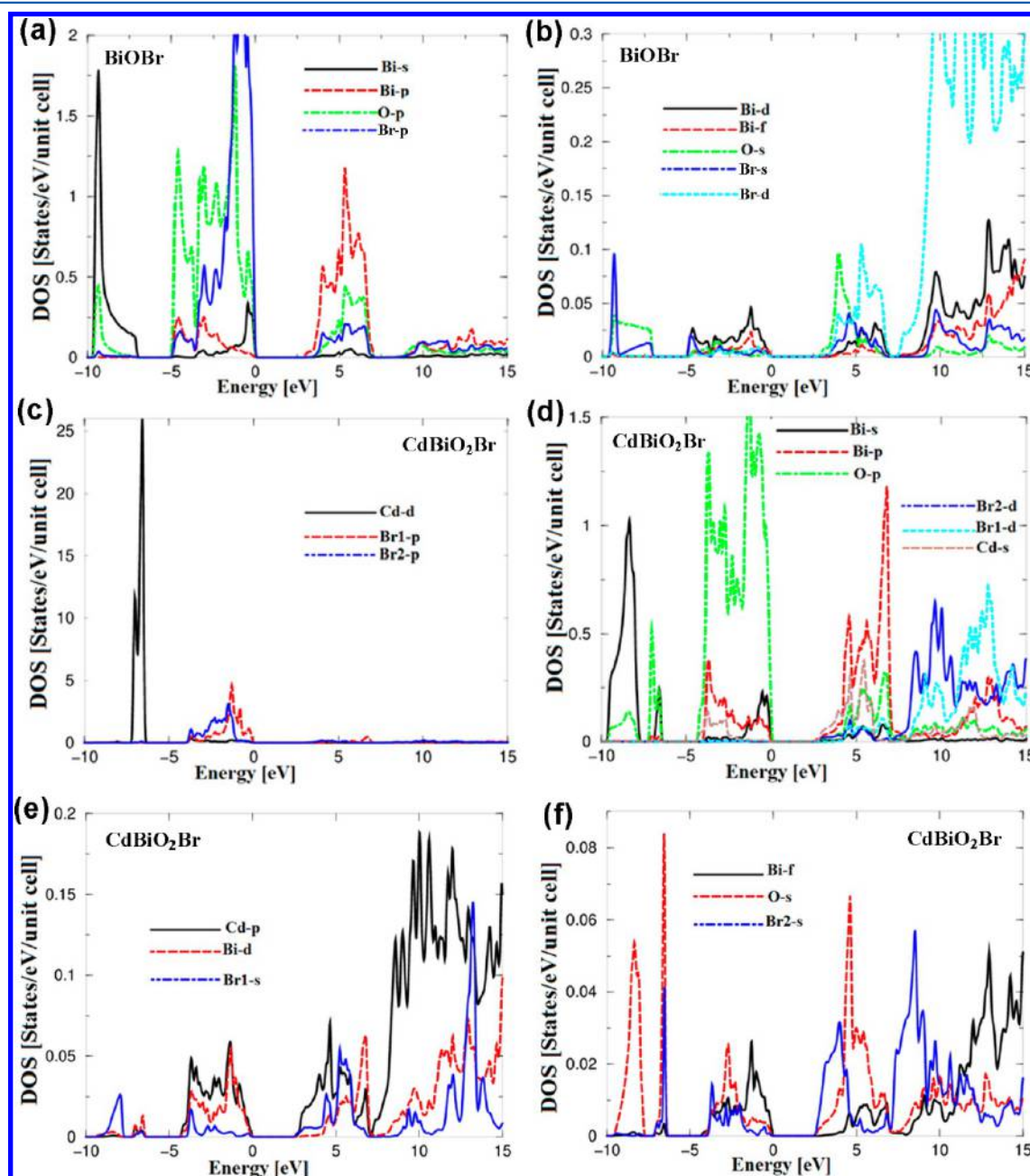
For understanding the movement behavior of photoinduced e$^-$ and h$^+$ from CdBiO$_2$Br and BiOBr, their angular momentum projected density of states are investigated as shown in Figure 9.[43] The valence band maximum (VBM) of BiOBr is composed

Figure 8. Transient photocurrent response of CdBiO$_2$Br and BiOBr with visible light irradiation (λ > 420 nm).
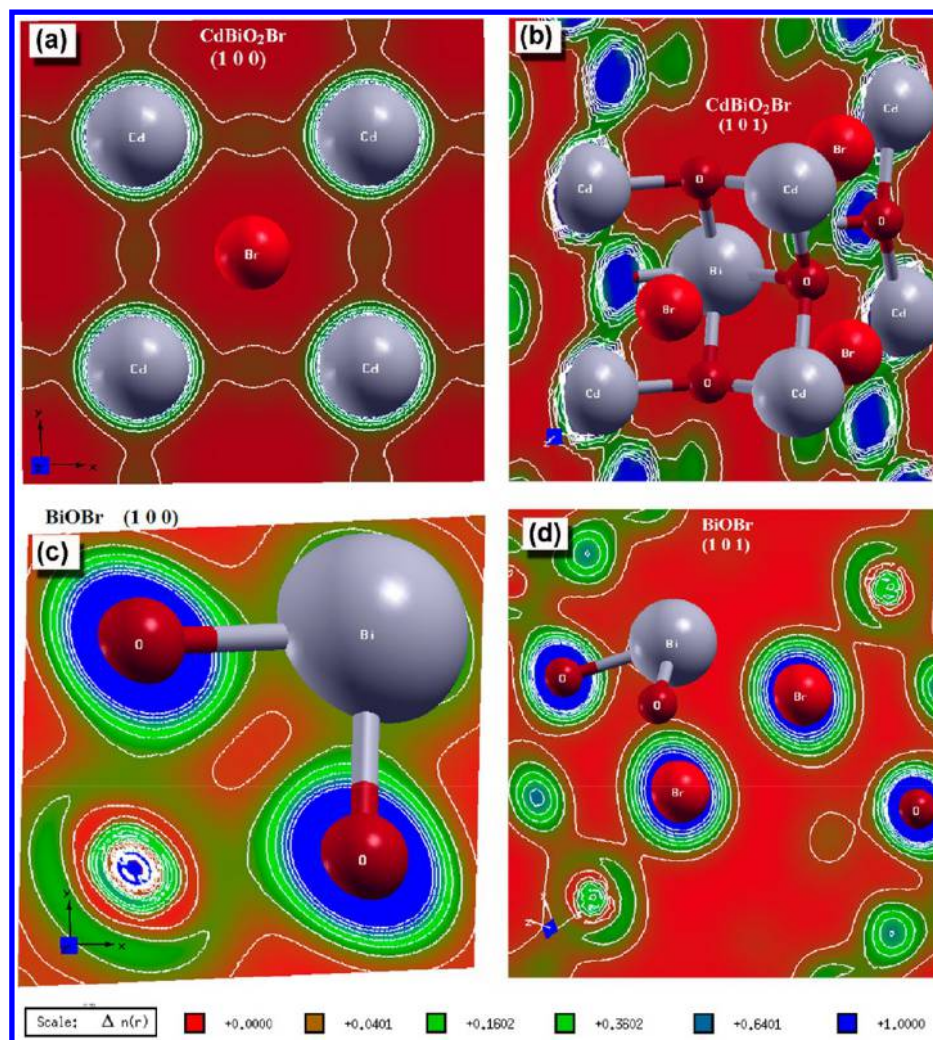
of Br 6p, Bi 6s, and O 2p with a tiny amount of Bi 5d and 4f states (Figure 9, parts a and b), and the VBM of CdBiO$_2$Br mainly consists of Br 6p, O 2p, and Bi 6s states (Figure 9c–f). It is clear that the Br 6p states are dominantly responsible for constructing the VBM for both CdBiO$_2$Br and BiOBr that could induce relatively localized photogenerated holes. With regard to conduction band maximum (CBM), it is mainly formed by Cd 5s and Bi 6p for CdBiO$_2$Br and by Bi 6p with a small amount of O 2s for BiOBr, respectively. That is, the photogenerated e$^-$ will jump to the Cd 5s and Bi 6p or Bi 6p orbitals, and the h$^+$ will move to the Br 6p orbital during the photocatalytic process.

The angular momentum projected density of states can indicate the presence of strong hybridization between the states. The state hybridization may give rise to formation of

Figure 9. Angular momentum projected density of states (DOS) of (a, b) BiOBr and (c–f) CdBiO$_2$Br.

Figure 10. (a) Calculated differential charge density of (a, b) CdBiO$_2$Br and (c, d) BiOBr along (100) and (101) planes.

covalent bonding, which depends on the degree of the hybridization. Compared with the ionic bonding, the covalent bonding is more favorable for the transport of charge carriers.[44] To corroborate this statement and to uncover the chemical bonding properties of CdBiO$_2$Br and BiOBr, their electronic charge density is calculated in two crystallographic planes: (100) and (101) as shown in Figure 10. The charge localizes mainly between Cd and the neighboring O atoms, also between Bi and O atoms indicating a partial ionic and strong covalent bonding (Figure 10, parts a and b) in contrast to that of BiOBr (Figure 10, parts c and d). The strength of the interactions between the atoms is due to the degree of the hybridization and the electronegativity differences. According to Pauling scale, the electronegativity of Cd, Bi, O and Br are 1.69, 2.02, 3.44 and 2.96, respectively. To describe the character of the chemical bonding in CdBiO$_2$Br and BiOBr, the difference in electronegativity ($X_A - X_B$) is crucial; herein, X_A and X_B represent the electronegativity of A and B atoms in general. With a rise in the the $X_A - X_B$ value, the ionic character (P) of the bonding increases. The percentage of P for the chemical bonding can be obtained using the expression:

$$P \; (\%) = 16(X_A - X_B) + 3.5(X_A - X_B)^2 \qquad (1)$$

The calculated values of P are given in Table S2. It is clear that the Cd−O, Bi−O, Cd−Br, and Bi−Br bonds are mostly covalent and partially ionic bonding. The covalent bonding is more favorable for the transport of the carriers than ionic bonding.[44]

The mobility of the photogenerated carriers significantly influences the photoinduced ROS evolution, and the effective mass provides essential information to understand the photocatalytic mechanism.[45] To gain in-depth insight into the movement status of photoinduced e$^-$ and h$^+$, the effective masses of charge carriers of CdBiO$_2$Br and BiOBr are quantitatively calculated as shown in Table 2. The effective

Table 2. Calculated Effective Masses of Carriers for CdBiO$_2$Br and BiOBr

	m_e^*/m_o	m_h^*/m_o	$D(m_e^*/m_h^*)$
CdBiO$_2$Br	0.0154	0.0077	2.00
BiOBr	0.0218	0.0229	0.95

masses of carriers are calculated by the second derivative of the bottom point for the CB position and the top point for the VB position based on $E = h^2k^2/\, 2m_e m^*$; here m_e represents the mass of free electron (9.1×10^{-19} kg). It is evident that the effective masses of e$^-$ and h$^+$ of CdBiO$_2$Br are smaller than that of BiOBr, demonstrating that the mobility of both the e$^-$ and h$^+$ are higher in CdBiO$_2$Br compared to in BiOBr.[45] In

particular, the h$^+$ effective mass of CdBiO$_2$Br is only one-third of that of BiOBr, which corresponds to the far superior $^\bullet$OH production rate of CdBiO$_2$Br. Moreover, the effective mass difference ($D = m_e^*/m_h^*$) between electron (e) and hole (h) is also calculated. A large D reflects a significant difference in the respective mobility of e$^-$ and h$^+$, which is beneficial for efficient charge separation.[46] As displayed in Table 2, the D value of CdBiO$_2$Br and BiOBr is 2.00 and 0.95, respectively. The much greater D value of CdBiO$_2$Br indicates that the photogenerated e$^-$ and h$^+$ from CdBiO$_2$Br are more prone to separate and transfer along different directions, which are accounting for its more efficient oxygen activation performance.

Analysis on Relationship between Layer Structure and Photoinduced Charge Separation. To deep understand the charge separation difference originated from the crystal structures of CdBiO$_2$Br and BiOBr, their crystal configurations along the $b-c$ plane are depicted and compared in Figure 11. Because of the alternatively arranged positively
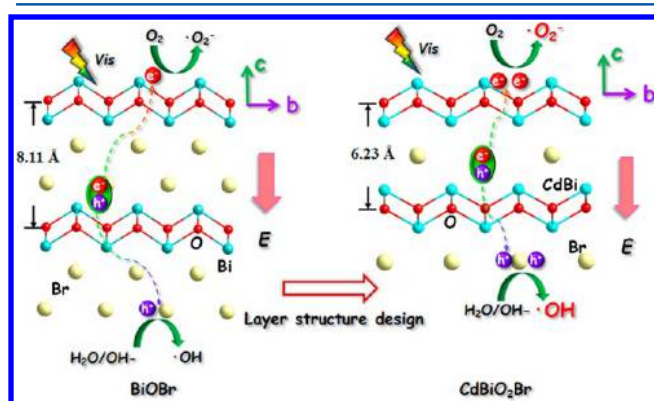
Figure 11. Schematic illustration for layer structure evolution from BiOBr to CdBiO$_2$Br and their respective charge separation and oxygen activation processes.

charged [CdBiO$_2$]$^+$ or [Bi$_2$O$_2$]$^{2+}$ layers and negatively charged Br$^-$ slices, there exists an internal self-built electric field between the layers along the c axis, which can promote the migration of e$^-$ and h$^+$ along different directions. As revealed by the above calculated PDOS, during the photoexcitation process, the photogenerated e$^-$ will transfer onto the Cd 5s/Bi 6p orbitals for CdBiO$_2$Br and to Bi 6p orbital for BiOBr, and meanwhile the h$^+$ moves to the Br 4p orbital for both. In other words, the photogenerated e$^-$ would migrate to the [CdBiO$_2$]$^+$ or [Bi$_2$O$_2$]$^{2+}$ layers, and the h$^+$ transfers to the Br$^-$ slices. The photogenerated e$^-$ in [CdBiO$_2$]$^+$/[Bi$_2$O$_2$]$^{2+}$ layers will reduce O$_2$ molecules to produce superoxide radicals ($^\bullet$O$_2^-$), and h$^+$ in Br$^-$ slices will transform H$_2$O or OH$^-$ into hydroxyl radicals ($^\bullet$OH) through oxidation reaction. Thus, the distance between [CdBiO$_2$]$^+$/[Bi$_2$O$_2$]$^{2+}$ layers and Br$^-$ slices, namely, the diffusion path of carriers, is a very crucial factor to determine the mobility efficiency of e$^-$ and h$^+$ as well as molecular oxygen activation capability. In BiOBr, the interlayer spacing between two adjacent [Bi$_2$O$_2$]$^{2+}$ layers is 8.11 Å, and thus each Br$^-$ slice has an average distance of 4.06 Å from its first [Bi$_2$O$_2$]$^{2+}$ layer neighbors. With regard to CdBiO$_2$Br, the distance between [CdBiO$_2$]$^+$ layers and interbedded Br$^-$ slices is 3.12 Å (one-half of that between two adjacent [CdBiO$_2$]$^+$ layers (6.23 Å)). Apparently, the much shorter diffusion path in CdBiO$_2$Br than that in BiOBr allows the photogenerated e$^-$ and h$^+$ favorable migration to the surface of the catalysts, namely the e$^-$ and h$^+$

from CdBiO$_2$Br has a higher mobility. This is consistent with the above theoretical results that the effective masses of e$^-$ and h$^+$ of CdBiO$_2$Br are smaller than that of BiOBr. Consequently, CdBiO$_2$Br holds a more powerful ability in oxygen activation for generating more abundant $^\bullet$O$_2^-$ and $^\bullet$OH. Though the internal self-built electric field in BiOBr may be stronger than that of CdBiO$_2$Br owing to the higher opposite charges of neighboring layers, the interlayer spacing clearly takes a more dominating role in contributing to the separation and migration of photoinduced e$^-$-h$^+$ pairs. It is also demonstrated that the layer structure designs are highly effective for promoting charge separation and oxygen activation reactions.

CONCLUSIONS

In summary, Sillén-structured mixed-cationic layered CdBiO$_2$Br nanosheets with visible-light response were developed by a facile hydrothermal assembly route. The crystal structure of CdBiO$_2$Br consists of [CdBiO$_2$]$^+$ layers and alternatively interbedded single Br$^-$ slice. This structural feature allows CdBiO$_2$Br a narrower interlayer spacing than BiOBr. Density of states calculations uncover that the diffusion of photogenerated electrons (e$^-$) and holes (h$^+$) occurs between the [CdBiO$_2$]$^+$/[Bi$_2$O$_2$]$^{2+}$ and Br$^-$ layers, and thus the diffusion paths of charge carriers were shortened in CdBiO$_2$Br. ESR experiments demonstrated that CdBiO$_2$Br far outperforms BiOBr in producing superoxide radicals ($^\bullet$O$_2^-$) and hydroxyl radicals ($^\bullet$OH) with illumination of visible light, and the oxygen species evolution rates are ~2.4 and 14.1 times that of BiOBr. In depth calculation results disclose that CdBiO$_2$Br not only has smaller effective masses for both e$^-$ and h$^+$ of than BiOBr, but also shows a larger effective mass difference, indicating the efficient mobility and separation of charge carriers in CdBiO$_2$Br. The current study advances our knowledge on the relationship between layered crystal structure and charge separation/ photoreactivity, and may be potentially extended to develop high-performance layered materials applied in other fields, such as lithium-ion batteries, supercapacitors, etc.

ASSOCIATED CONTENT

Ⓢ Supporting Information

The Supporting Information is available free of charge on the ACS Publications website at DOI: 10.1021/acs.jpcc.7b08661.

> XRD pattern and SEM image of CdBiO$_2$Br, fractional atomic coordinates, occupancies and isotropic thermal parameters of CdBiO$_2$Br obtained from the Rietveld Refinement, and the calculated values of the ionic character (PDF)

AUTHOR INFORMATION

Corresponding Author
*(H.H.) E-mail: hhw@cugb.edu.cn. Telephone: +86-010-82332247.

ORCID 🄾
Hongwei Huang: 0000-0003-0271-1079
Ali H. Reshak: 0000-0001-9426-8363
Yihe Zhang: 0000-0002-1407-4129

Notes
The authors declare no competing financial interest.

■ REFERENCES

(1) Kubacka, A.; Fernández-García, M.; Colón, G. Advanced Nanoarchitectures for Solar Photocatalytic Applications. *Chem. Rev.* **2012**, *112*, 1555−1614.

(2) Feng, M. L.; Sarma, D.; Qi, X. H.; Du, K. Z.; Huang, X. Y.; Kanatzidis, M. G. Efficient Removal and Recovery of Uranium by a Layered Organic−Inorganic Hybrid Thiostannate. *J. Am. Chem. Soc.* **2016**, *138*, 12578−12585.

(3) Zhao, Y. F.; Chen, G. B.; Bian, T.; Zhou, C.; Waterhouse, G. I. N.; Wu, L. Z.; Tung, C. H.; Smith, L. J.; O'Hare, D.; Zhang, T. R. Defect-Rich Ultrathin ZnAl-Layered Double Hydroxide Nanosheets for Efficient Photoreduction of CO_2 to CO with Water. *Adv. Mater.* **2015**, *27*, 7823−7823.

(4) Zhou, X.; Cheng, J. X.; Zhou, Y. B.; Cao, T.; Hong, H.; Liao, Z. M.; Wu, S. W.; Peng, H. L.; Liu, K. H.; Yu, D. P. Strong Second-Harmonic Generation in Atomic Layered GaSe. *J. Am. Chem. Soc.* **2015**, *137*, 7994−7997.

(5) Li, J.; Li, H.; Zhan, G. M.; Zhang, L. Z. Solar Water Splitting and Nitrogen Fixation with Layered Bismuth Oxyhalides. *Acc. Chem. Res.* **2017**, *50*, 112−121.

(6) Guan, M.; Xiao, C.; Zhang, J.; Fan, S.; An, R.; Cheng, Q.; Xie, J.; Zhou, M.; Ye, B.; Xie, Y. Vacancy Associates Promoting Solar-driven Photocatalytic Activity of Ultrathin Bismuth Oxychloride Nanosheets. *J. Am. Chem. Soc.* **2013**, *135*, 10411−10417.

(7) Cheng, H. F.; Huang, B. B.; Dai, Y. Engineering BiOX (X = Cl, Br, I) Nanostructures for Highly Efficient Photocatalytic Applications. *Nanoscale* **2014**, *6*, 2009−2026.

(8) Huang, H. W.; Li, X. W.; Wang, J. J.; Dong, F.; Chu, P. K.; Zhang, T. R.; Zhang, Y. H. Anionic Group Self-Doping as a Promising Strategy: Band-Gap Engineering and Multi-Functional Applications of High-Performance CO_3^{2-} Doped $Bi_2O_2CO_3$. *ACS Catal.* **2015**, *5*, 4094−4103.

(9) Fujito, H.; Kunioku, H.; Kato, D.; Suzuki, H.; Higashi, M.; Kageyama, H.; Abe, R. Layered Perovskite Oxychloride Bi_4NbO_8Cl: A Stable Visible Light Responsive Photocatalyst for Water Splitting. *J. Am. Chem. Soc.* **2016**, *138*, 2082−2085.

(10) Zhou, Y. G.; Zhang, Y. F.; Lin, M. S.; Long, J. L.; Zhang, Z. Z.; Lin, H. X.; Wu, J. C. S.; Wang, X. X. Monolayered Bi_2WO_6 Nanosheets Mimicking Heterojunction Interface with Open Surfaces for Photocatalysis. *Nat. Commun.* **2015**, *6*, 8340.

(11) Bai, X. J.; Wang, L.; Zhu, Y. F. Visible Photocatalytic Activity Enhancement of $ZnWO_4$ by Graphene Hybridization. *ACS Catal.* **2012**, *2*, 2769−2778.

(12) Huang, H. W.; Cao, R. R.; Yu, S. X.; Xu, K.; Hao, W. C.; Wang, Y. G.; Dong, F.; Zhang, T. R.; Zhang, Y. H. Single-Unit-Cell Layer Established Bi_2WO_6 3D Hierarchical Architectures: Efficient Adsorption, Photocatalysis and Dye-Sensitized PhotoelectroChemical Performance. *Appl. Catal., B* **2017**, *219*, 526−537.

(13) Li, J.; Yu, Y.; Zhang, L. Z. Bismuth Oxyhalide Nanomaterials: Layered Structures Meet Photocatalysis. *Nanoscale* **2014**, *6*, 8473−8488.

(14) Huang, H. W.; Han, X.; Li, X. W.; Wang, S. C.; Chu, P. K.; Zhang, Y. H. Fabrication of Multiple Heterojunctions with Tunable Visible-Light-Active Photocatalytic Reactivity in BiOBr-BiOI Full-Range Composites Based on Microstructure Modulation and Band Structures. *ACS Appl. Mater. Interfaces* **2015**, *7*, 482−492.

(15) Huang, H. W.; Xiao, K.; He, Y.; Zhang, T. R.; Dong, F.; Du, X.; Zhang, Y. H. In Situ Assembly of $BiOI@Bi_{12}O_{17}Cl_2$ p-n Junction: Charge Induced Unique Front-Lateral Surfaces Coupling Heterostructure with High Exposure of BiOI {001} Active Facets for Robust and Nonselective Photocatalysis. *Appl. Catal., B* **2016**, *199*, 75−86.

(16) Yin, S.; Wu, T.; Li, M.; Di, J.; Ji, M. X.; Wang, B.; Chen, Y.; Xia, J. X.; Li, H. M. Controllable Synthesis of Perovskite-like $PbBiO_2Cl$ Hollow Microspheres with Enhanced Photocatalytic Activity for Antibiotic Removal. *CrystEngComm* **2017**, *19*, 4777−4788.

(17) Shan, Z. C.; Wang, W. D.; Lin, X. P.; Ding, H. M.; Huang, F. Q. Photocatalytic Degradation of Organic Dyes on Visible-light Responsive Photocatalyst $PbBiO_2Br$. *J. Solid State Chem.* **2008**, *181*, 1361−1366.

(18) Zou, Z.; Ye, J.; Arakawa, H. Substitution Effects of In^{3+} by Fe^{3+} on Photocatalytic and Structural Properties of Bi_2InNbO_7 Photocatalysts. *J. Mol. Catal. A: Chem.* **2001**, *168*, 289−297.

(19) Huang, H. W.; He, Y.; Li, X. W.; Li, M.; Zeng, C.; Dong, F.; Du, X.; Zhang, T. R.; Zhang, Y. H. Non-Centrosymmetric $Bi_2O_2(OH)$-(NO_3) as a Desirable $[Bi_2O_2]^{2+}$ Layered Photocatalyst: Strong Intrinsic Polarity, Rational Band Structure and {001} Active Exposing Facets Co-Benefiting for Robust Photooxidating Capability. *J. Mater. Chem. A* **2015**, *3*, 24547−24556.

(20) Huang, H. W.; He, Y.; Lin, Z. S.; Kang, L.; Zhang, Y. H. Two Novel Bi-Based Borate Photocatalysts: Crystal Structure, Electronic Structure, Photoelectrochemical Properties, and Photocatalytic Activity under Simulated Solar Light Irradiation. *J. Phys. Chem. C* **2013**, *117*, 22986−22994.

(21) Huang, H. W.; Xiao, K.; Zhang, T. R.; Dong, F.; Zhang, Y. H. Rational Design on 3D Hierarchical Bismuth Oxyiodides via In Situ Self-template Phase Transformation and Phase-junction Construction for Optimizing Photocatalysis Against Diverse Contaminants. *Appl. Catal., B* **2017**, *203*, 879−888.

(22) Ye, K. H.; Chai, Z. S.; Gu, J. W.; Yu, X.; Zhao, C. X.; Zhang, Y. M.; Mai, W. J. $BiOI-BiVO_4$ Photoanodes with Significantly Improved Solar Water Splitting Capability: p−n Junction to Expand Solar Adsorption Range and Facilitate Charge Carrier Dynamics. *Nano Energy* **2015**, *18*, 222−231.

(23) Huang, H. W.; Xiao, K.; Du, X.; Zhang, Y. H. Vertically Aligned Nanosheets-Array-like BiOI Homojunction: Three-in-One Promoting Photocatalytic Oxidation and Reduction Abilities. *ACS Sustainable Chem. Eng.* **2017**, *5*, 5253−5264.

(24) Tu, S. C.; Huang, H. W.; Zhang, T. R.; Zhang, Y. H. Controllable Synthesis of Multi-Responsive Ferroelectric Layered Perovskite-Like $Bi_4Ti_3O_{12}$: Photocatalysis and Piezoelectric-Catalysis and Mechanism Insight. *Appl. Catal., B* **2017**, *219*, 550−562.

(25) Aliev, A.; Olchowka, J.; Colmont, M.; Capoen, E.; Wickleder, C.; Mentré, O. New $[PbBi_2O_4][Bi_2O_2]Cl_2$ and $[Pb_nBi_{10-n}O_{13}]$-$[Bi_2O_2]_nCl_{4+n}$ Series by Association of Sizable Subunits: Relationship with Arppe's Compound $Bi_{24}O_{31}Cl_{10}$ and Luminescence Properties. *Inorg. Chem.* **2013**, *52*, 8427−8435.

(26) Kennard, M. A.; Darriet, J.; Grannec, J.; Tressaud, A. Cation Ordering in the Sillén X1-Type Oxychloride, $BaBiO_2Cl$. *J. Solid State Chem.* **1995**, *117*, 201−205.

(27) Huang, H. W.; Liu, L. J.; Jin, S. F.; Yao, W. J.; Zhang, Y. H.; Chen, C. T. Deep-Ultraviolet Nonlinear Optical Materials: $Na_2Be_4B_4O_{11}$ and $LiNa_5Be_{12}B_{12}O_{33}$. *J. Am. Chem. Soc.* **2013**, *135*, 18319−18322.

(28) Yu, H. W.; Wu, H. P.; Pan, S. L.; Yang, Z. H.; Hou, X. L.; Su, X.; Jing, Q.; Poeppelmeier, K. R.; Rondinelli, J. M. $Cs_3Zn_6B_9O_{21}$: A Chemically Benign Member of the KBBF Family Exhibiting the Largest Second Harmonic Generation Response. *J. Am. Chem. Soc.* **2014**, *136*, 1264−1267.

(29) Zhao, S. G.; Kang, L.; Shen, Y. G.; Wang, X. D.; Asghar, M. A.; Lin, Z. S.; Xu, Y. Y.; Zeng, S. Y.; Hong, M. C.; Luo, J. H. Designing a Beryllium-Free Deep-Ultraviolet Nonlinear Optical Material without a Structural Instability Problem. *J. Am. Chem. Soc.* **2016**, *138*, 2961−2964.

(30) Zhao, K.; Zhang, L. Z.; Wang, J. J.; Li, Q. X.; He, W. W.; Yin, J. J. Surface Structure-Dependent Molecular Oxygen Activation of BiOCl Single-Crystalline Nanosheets. *J. Am. Chem. Soc.* **2013**, *135*, 15750−15753.

(31) Li, Y.; Zhang, W.; Niu, J. F.; Chen, Y. S. Mechanism of Photogenerated Reactive Oxygen Species and Correlation with the

Antibacterial Properties of Engineered Metal-Oxide Nanoparticles. *ACS Nano* **2012**, *6*, 5164−5173.

(32) Huang, H. W.; Tu, S. T.; Zeng, C.; Zhang, T. R.; Reshak, A. H.; Zhang, Y. H. Macroscopic Polarization Enhancement Promoting Photo- and Piezoelectric-Induced Charge Separation and Molecular Oxygen Activation. *Angew. Chem., Int. Ed.* **2017**, *56*, 11860−11864.

(33) Payne, M. C.; Teter, M. P.; Allan, D. C.; Arias, T. A.; Joannopoulos, J. D. Iterative Minimization Techniques for *ab initio* Total-energy Calculations: Molecular Dynamics and Conjugate Gradients. *Rev. Mod. Phys.* **1992**, *64*, 1045−1097.

(34) Clark, S. J.; Segall, M. D.; Pickard, C. J.; Hasnip, P. J.; Probert, M. J.; Refson, K.; Payne, M. C. First Principles Methods Using CASTEP. *Z. Kristallogr. - Cryst. Mater.* **2005**, *220*, 567−570.

(35) Blöchl, P. E.; Jepsen, O.; Andersen, O. K. Improved Tetrahedron Method for Brillouin-Zone Integrations. *Phys. Rev. B: Condens. Matter Mater. Phys.* **1994**, *49*, 16223.

(36) Sillén, L. G. Roentgenuntersuchung von $LiBi_3O_4Cl_2$ und verwandten Stoffen. *Zeitschrift für anorganische und allgemeine Chemie* **1939**, *242*, 41−46.

(37) Olchowka, J.; Kabbour, H.; Colmont, M.; Adlung, M.; Wickleder, C.; Mentré, O. $ABiO_2X$ (A = Cd, Ca, Sr, Ba, Pb; X = halogen) Sillen X1 Series: Polymorphism Versus Optical Properties. *Inorg. Chem.* **2016**, *55*, 7582−7592.

(38) Huang, H. W.; He, Y.; Du, X.; Chu, P. K.; Zhang, Y. H. A General and Facile Approach to Heterostructured Core/Shell $BiVO_4$/BiOI p-n Junction: Room-Temperature In Situ Assembly and Highly Boosted Visible-Light Photocatalysis. *ACS Sustainable Chem. Eng.* **2015**, *3*, 3262−3273.

(39) Guo, Y. X.; Huang, H. W.; He, Y.; Tian, N.; Zhang, T. R.; Chu, P. K.; An, Q.; Zhang, Y. H. In Situ Crystallization for Fabrication of Core-satellites structured BiOBr-CdS Heterostructure with an Excellent Visible−Light-Responsive Photoreactivity. *Nanoscale* **2015**, *7*, 11702−11711.

(40) Xu, M. C.; Gao, Y. K.; Moreno, E. M.; Kunst, M.; Muhler, M.; Wang, Y.; Idriss, H.; Wöll, C. Photocatalytic Activity of Bulk TiO_2 Anatase and Rutile Single Crystals Using Infrared Absorption Spectroscopy. *Phys. Rev. Lett.* **2011**, *106*, 138302.

(41) Wan, Z.; Zhang, G. K.; Wu, X. Y.; Yin, S. Novel Visible-Light-Driven Z-scheme $Bi_{12}GeO_{20}$/g-C_3N_4 Photocatalyst: Oxygen-Induced Pathway of Organic Pollutants Degradation and Proton Assisted Electron Transfer Mechanism of Cr(VI) Reduction. *Appl. Catal., B* **2017**, *207*, 17−26.

(42) Li, Y. X.; Ouyang, S. X.; Xu, H.; Wang, X.; Bi, Y. P.; Zhang, Y. F.; Ye, J. H. Constructing Solid−Gas-Interfacial Fenton Reaction over Alkalinized-C_3N_4 Photocatalyst to Achieve Apparent Quantum Yield of 49% at 420 nm. *J. Am. Chem. Soc.* **2016**, *138*, 13289−13297.

(43) Sun, Z. Y.; Zhang, L.; Dang, F.; Liu, Y.; Fei, Z. Y.; Shao, Q.; Lin, H.; Guo, J.; Xiang, L. C.; Yerra, N.; Guo, Z. H. Experimental and Simulation-Based Understanding of Morphology Controlled Barium Titanate Nanoparticles under Co-adsorption of Surfactants. *CrystEngComm* **2017**, *19*, 3288−3298.

(44) Wu, F.; Song, H. Z.; Jia, J. F.; Hu, X. Effects of Ce, Y, and Sm Doping on the Thermoelectric Properties of Bi_2Te_3 Alloy. *Prog. Nat. Sci.* **2013**, *23*, 408−412.

(45) Le Bahers, T.; Rerat, M.; Sautet, P. Semiconductors Used in Photovoltaic and Photocatalytic Devices: Assessing Fundamental Properties from DFT. *J. Phys. Chem. C* **2014**, *118*, 5997−6008.

(46) Yang, J.; Jiang, P. F.; Yue, M. F.; Yang, D. F.; Cong, R. G.; Gao, W. L.; Yang, T. $Bi_2Ga_4O_9$: An Undoped Single-Phase Photocatalyst for Overall Water Splitting under Visible Light. *J. Catal.* **2017**, *345*, 236−244.